catalysts

MDPI

Article

Enhancing the Catalytic Activity of *Candida antarctica* Lipase B (CALB) for the Synthesis of Moxifloxacin Intermediates by Loop Engineering

Sining Wei [1], Mahwish Aziz [2], Yilin Zhang [3], Jian Xiong [1,*], Cheng Cheng [2,*] and Bin Wu [2]

[1] College of Chemistry and Chemical Engineering, Henan University of Science and Technology, Luoyang 471023, China; 230320251434@stu.haust.edu.cn
[2] College of Biotechnology and Pharmaceutical Engineering, Nanjing Tech University, Nanjing 211816, China; mahwishaziz15@gmail.com (M.A.); wubin1977@njtech.edu.cn (B.W.)
[3] Taian Havay Chemicals Co., Ltd., Taian Dawenkou Gypsum Industry Park, Taian 271000, China; jack685168@163.com
* Correspondence: xiongjian@haust.edu.cn (J.X.); cheng2@njtech.edu.cn (C.C.)

Abstract

This study addressed the issue of insufficient activity in CALB lipase during the catalytic synthesis of key chiral intermediates for moxifloxacin. A structure-guided protein engineering strategy was employed to systematically modify its functional domains. Through molecular dynamics simulations of CALB-I189K, multiple regions exhibiting high conformational flexibility were preliminarily identified. Subsequently, by integrating 3D structural alignment with active site pocket distance analysis, the functionally most critical region (143–146) was selected. A site-directed saturation mutation library was constructed specifically targeting this region. Building upon the previously reported CALB-I189K, a mutant I189K/L144R/A146K was ultimately obtained through high-throughput screening combined with chiral HPLC validation. This mutant maintains excellent stereoselectivity (E = 206.52) while enhancing catalytic efficiency (k_{cat}/K_m) to 273.73 $min^{-1}\cdot mM^{-1}$, approximately 4.5-fold that of I189K. At a substrate concentration of 1 M, it achieves 50% conversion within 2.6 h, demonstrating kinetic resolution capabilities approaching industrial standards. Molecular simulation analysis indicates that the L144R and A146K mutations synergistically enhance catalytic performance primarily by optimizing spatial distances between catalytic residues. This study not only provides a high-performance catalyst for the efficient biosynthesis of moxifloxacin chiral intermediates but also offers new insights for enzyme rational design based on dynamic structural information.

Keywords: moxifloxacin; *Candida antarctica* lipase B; molecular modification; kinetic resolution

Check for updates

Academic Editors: David D. Boehr, Katja S. Johansen and Kristian B.R.M. Krogh

Received: 18 March 2026
Revised: 13 April 2026
Accepted: 18 April 2026
Published: 24 April 2026

Copyright: © 2026 by the authors. Licensee MDPI, Basel, Switzerland. This article is an open access article distributed under the terms and conditions of the Creative Commons Attribution (CC BY) license.

1. Introduction

Moxifloxacin is a new-generation fluoroquinolone antibiotic that is commonly used in clinical settings. It is known for its excellent penetration into lung tissue and strong effectiveness against various respiratory pathogens. Compared to earlier generations of quinolone antibiotics, Moxifloxacin offers a significant improvement in its antimicrobial spectrum, pharmacological properties, and safety profile [1,2]. (*S*,*S*)-2,8-Diazabicyclo [4.3.0]nonane (4, as shown in Figure 1) is a crucial chiral intermediate in the synthesis of moxifloxacin. However, producing this compound is challenging due to the presence of two stereogenic centers. Various chemical synthetic routes have been developed to obtain compound 4,

but these methods often face common limitations, including low efficiency in resolution, high costs for starting materials, and reliance on metal catalysts [3–5]. Currently, two enzymatic routes have been reported for the synthesis of compound 4: (i) lipase-mediated resolution of racemic *cis*-(±)-dimethyl-1-acetylpiperidine-2,3-dicarboxylate (*cis*-(±)-1) [6] and (ii) transaminase-catalyzed resolution of 4-(3-chloropropyl)-3-pyrrolidinone and its derivatives [7]. Among these methods, the lipase-based approach stands out because it utilizes the kinetic resolution of *cis*-(±)-1 to produce (2*S*,3*R*)-dimethyl-1-acetylpiperidine-2,3-dicarboxylate ((2*S*,3*R*)-1). This method is particularly attractive due to its excellent stereoselectivity, with an E value greater than 2000 [6] (Figure 1). Ramesh et al. [8] reported that 80 g/L of *cis*-(±)-1 was completely resolved by 40 g/L immobilized *Candida antarctica* lipase B (CALB) in buffer solution (pH 6.0) at 35 °C. However, this reaction required an extended duration of 140 h. Subsequently, Cai et al. [9] discovered that *Sporisorium reilianum* lipase (SRL) also demonstrated strict stereoselectivity toward *cis*-(±)-1. Nevertheless, the poor catalytic activity of lipases toward *cis*-(±)-1 significantly limits the practical applicability of this process.

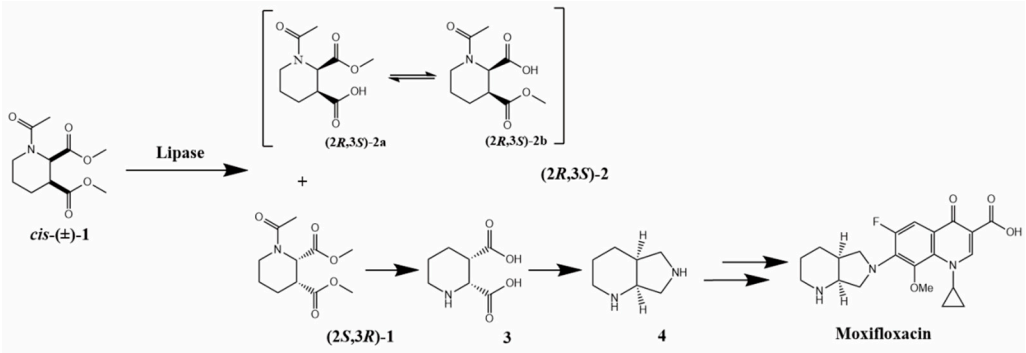


Figure 1. A chemo-enzymatic synthesis of moxifloxacin was achieved via lipase-catalyzed kinetic resolution of *cis*-(±)-1, followed by chemical transformation of the resulting (2*S*,3*R*)-1 to prepare the chiral intermediate of moxifloxacin.

Protein engineering has emerged as a powerful tool with numerous successes in improving catalytic functions of lipases [10–12]. For example, Shen et al. [13] applied a combinatorial active-site saturation test in conjunction with site-directed saturation mutagenesis to remodel the substrate-binding pocket and access channel. This work resulted in enhanced catalytic activity of CALB towards *cis*-(±)-1. The best variant, I189K, demonstrated a remarkable 286-fold increase in catalytic activity compared to CALB. Additionally, the lipase SRL was engineered using site-saturation mutagenesis and combinatorial mutagenesis, leading to a significant enhancement in catalytic activity towards *cis*-(±)-1. This improvement resulted in an increase from barely detectable levels to 87.8 U/mg [9]. For the industrial biosynthesis of moxifloxacin, an efficient resolution of *cis*-(±)-1 is necessary, which requires higher substrate loading, reduced enzyme usage, and shortened reaction times.

This study employed a structure-guided focused combinatorial mutagenesis strategy to engineer CALB-I189K. Through molecular dynamics simulations of CALB-I189K, multiple regions exhibiting high conformational flexibility were preliminarily identified (143–146, 188–190, 242–252, 278–285). Subsequently, integrating 3D structural alignment with active pocket distance analysis, the functionally critical 143–146 region was selected for targeted saturation mutagenesis library construction. Using the previously reported I189K mutant as a template, combined with high-throughput colorimetric screening and chiral HPLC validation, the composite I189K/L144R/A146K mutant was ultimately obtained. This mutant maintains excellent stereoselectivity while significantly enhancing catalytic

efficiency. This strategy achieves precise modification of the key functional Loop segment, providing a high-performance biocatalyst for the efficient synthesis of moxifloxacin chiral intermediates.

2. Results and Discussion

2.1. Mutant Library Design

In the field of enzyme protein engineering, constructing efficient and precise mutation libraries is crucial for reducing screening workload and experimental costs [14]. To rationally design such libraries, a deep understanding of key structural factors affecting enzyme function is required. To this end, we first predicted the three-dimensional structure of CALB-I189K and conducted a 100 ns molecular dynamics simulation. Results indicate that the root mean square deviation (RMSD) (Figure S1) reached equilibrium after approximately 40 ns. Consequently, we calculated the root mean square fluctuation (RMSF) of the protein backbone atoms for the final 30 ns (Figure 2a).

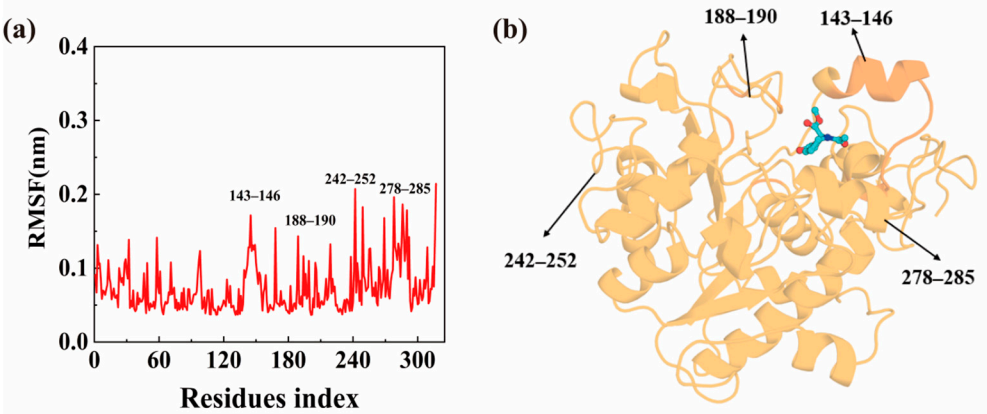


Figure 2. Conformation Dynamics Analysis and Key Structural Features of CAL-B-I189K: (**a**) RMSF of CAL-B-I189K molecular dynamics simulations; (**b**) spatial distribution of key flexible regions in the enzyme's three-dimensional structure.

Highly flexible regions within enzymes serve as critical structural foundations for conformational changes, closely linked to their activity and stability. Analyzing the dynamic evolution of enzyme conformations aids in identifying functionally critical hotspot residues [15–17]. RMSF analysis revealed significant fluctuation peaks in residue regions 143–146, 188–190, 242–252, and 278–285, indicating high conformational flexibility in these areas. Structural analysis confirmed that the 143–146 region resides within a critical functional Loop on the protein surface, directly participating in shaping the active site conformation (Figure 2b). According to research by Stauch et al. [18], the specific motion patterns of this Loop region are crucial for precise substrate recognition and binding. The 188–190 segment contains the known beneficial mutation site I189K. Although the 242–252 segment exhibits pronounced RMSF fluctuations, its distance from the active site limits its potential for modification. The 278–285 segment forms a helical structure adjacent to the active pocket [19,20]. Although it exhibits some conformational flexibility in simulations, it is generally not prioritized for modification. Notably, we also compared the RMSF of wild-type CALB with CALB-I189K and found that the I189K mutation significantly altered the flexibility of the relevant region (particularly 188–190 and its surroundings) (Figure S2). This result directly links the "known beneficial mutation" with "observable conformational dynamics," strongly supporting the critical impact of local flexibility changes on enzyme activity. This finding underpins our strategy of selecting engineering targets based on conformational dynamics.

Guided by the engineering principle that "highly flexible Loops near the active site are priority targets for modification [21]," and integrating RMSF and structural analysis from this study, we ultimately identified the 143–146 segment as a hotspot residue region. Using CALB-I189K as the initial template [13], we conducted systematic saturation mutagenesis experiments.

2.2. Construction and Screening of Mutants

Based on the selected region (143–146), we constructed site-saturated mutation libraries using the NNK codon degeneracy strategy. Through high-throughput screening of approximately 1700 transformants using the bromothymol blue colorimetric assay, 43 primary hits showing obvious color change (blue to yellow) were selected. All 43 were further analyzed by chiral HPLC, and 21 clones exhibited higher hydrolytic activity than I189K. After DNA sequencing, these 21 clones were found to represent five unique non-redundant beneficial single-site mutants: four at position L144 (L144R, L144S, L144E, L144M) and one at position A146 (A146K) (Figure S3). No significant beneficial mutations were identified at other sites. Subsequently, CALB-I189K and the screened positive mutants were expressed in shake flasks. After purification via Ni-NTA affinity chromatography, their hydrolytic conversion rates using *cis*-(±)-1 as substrate were determined by chiral HPLC, enabling accurate assessment of specific activity and enantioselectivity. Results showed that all five mutants exhibited enhanced activity compared to the initial I189K enzyme, while maintaining high enantioselectivity (E > 200) (Figure 3).

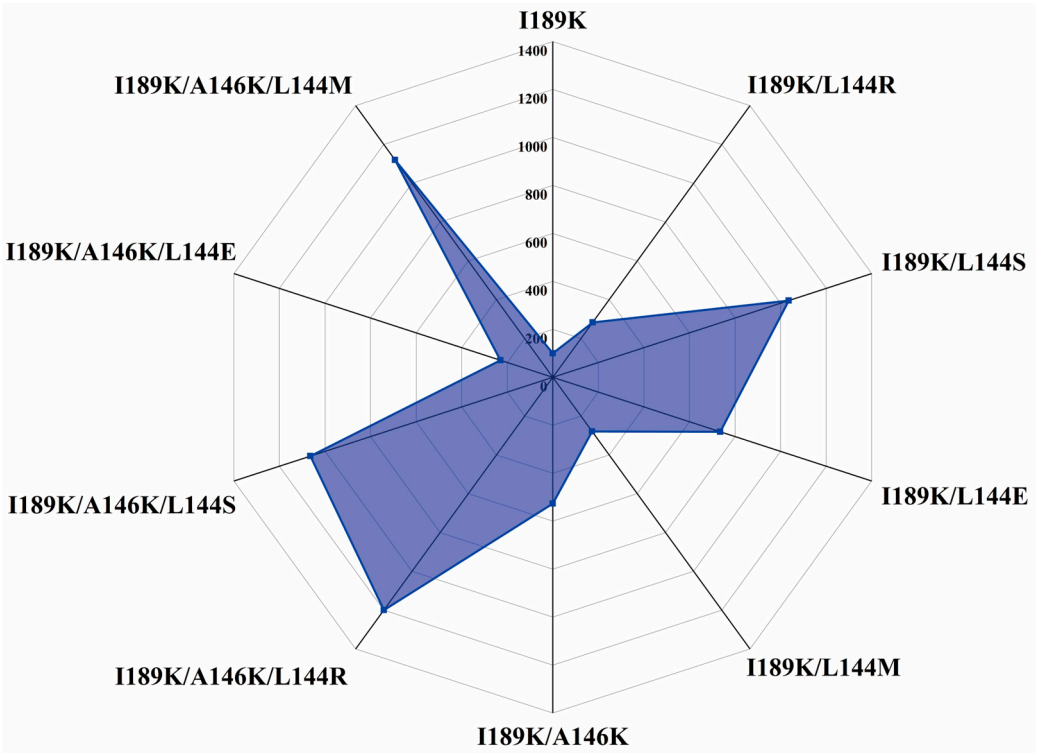


Figure 3. Enzyme Activity Comparison of CAL-B Mutants: Relative enzyme activity of L144 and A146 site mutants compared to I189K.

Furthermore, we systematically combined and evaluated the beneficial mutations described above. In the CALB-I189K background, the relative enzyme activities of mutants L144R, L144S, L144E, and L144M increased by 2.8-fold, 10.4-fold, 7.4-fold, and 2.8-fold, respectively, while mutant A146K increased by 5.3-fold. Building upon this foundation, the L144 site mutation was further introduced into the I189K/A146K background. The resulting mutants I189K/A146K/L144M, I189K/A146K/L144E, I189K/A146K/L144R,

and I189K/A146K/L144S exhibited relative enzyme activities increased to 11.2-fold, 2.3-fold, 12.0-fold, and 10.6-fold, respectively, without compromising enantiomeric selectivity (E > 200). For the best mutant I189K/L144R/A146K, its E value was determined to be 206.52.

It is worth emphasizing that previous literature reports indicate that a single mutation at the L144 site in the CALB wild-type did not yield variants with significantly enhanced activity [13]. However, when occurring in the context of the I189K mutation, the L144 mutation exhibited a pronounced gain-of-function effect, clearly demonstrating a synergistic effect. This result demonstrates that in protein engineering, the beneficial effects of individual mutations are highly dependent on their genetic background [22].

SDS-PAGE analysis confirmed the purity of the purified triple mutant, showing a single band at the expected molecular weight (33 kDa) with comparable intensity to that of I189K (Figure S4), and indicating similar expression and purification yields.

2.3. Kinetic Parameters of Mutants

Enzyme kinetic parameter measurements for key mutants further quantified their stepwise enhancement in catalytic performance (Table 1). Compared to the enzyme I189K, the catalytic efficiency (k_{cat}/K_m) of mutant I189K/L144R increased from 61.40 to 97.18, while the final mutant I189K/L144R/A146K reached 273.73, representing an approximately 4.5-fold increase in efficiency. This increase was primarily attributed to a dramatic rise in the k_{cat} value, which jumped from 1722.35 min^{-1} in the enzyme I189K to 11,617.28 min^{-1} in the I189K/L144R/A146K mutant, indicating a significant enhancement in the maximum substrate conversion rate per enzyme molecule. A concomitant phenomenon was the gradual increase in the K_m value from 28.05 mM to 42.44 mM, suggesting a weakening of the enzyme's apparent affinity for the substrate as mutations accumulated. Nevertheless, the substantial enhancement in k_{cat} fully offset the negative impact of affinity decline, ultimately driving the sustained optimization of overall catalytic efficiency. This kinetic profile demonstrates that the combination mutation strategy successfully optimized the enzyme's catalytic turnover process, providing a crucial kinetic foundation for achieving highly efficient industrial conversion.

Table 1. Kinetic parameters of the purified CAL-B variant for *cis*-(±)-1.

Enzyme	K_m (mM)	k_{cat} (min^{-1})	k_{cat}/K_m ($min^{-1} \cdot mM^{-1}$)
I189K	28.05 ± 1.90	1722.35 ± 76.64	61.40
I189K/L144R	36.89 ± 2.39	3585.14 ± 98.04	97.18
I189K/L144R/A146K	42.44 ± 3.98	11,617.28 ± 292.11	273.73

2.4. Effects of Temperature and pH on Mutant Enzyme Activity and Stability

The performance of enzymes in practical application environments is crucial for their industrial viability. This study systematically evaluated the temperature and pH adaptability of the final mutant I189K/L144R/A146K and compared it with that of the parent enzyme I189K to clarify its performance advantages and operational range.

As shown in Figure 4a, the optimal temperature for the mutant I189K/L144R/A146K was 35 °C, which is identical to the data for the parent enzyme I189K, and both values are lower than the wild-type CALB (40 °C) [13]. This indicates that the I189K mutation plays a dominant role in determining the enzyme's temperature preference, and the subsequent introduction of the L144R and A146K mutations did not alter this core characteristic. However, significant differences emerged in long-term thermal stability. As demonstrated by the 48 h incubation experiment in Figure 4b, the mutant I189K/L144R/A146K complex exhib-

ited a markedly faster activity decay rates at 35 °C compared to the parent enzyme I189K. This observation is consistent with the commonly reported "activity–stability trade-off" in protein engineering, whereby substantial gains in catalytic activity through combinatorial mutations are often accompanied by partial losses in structural stability [23].

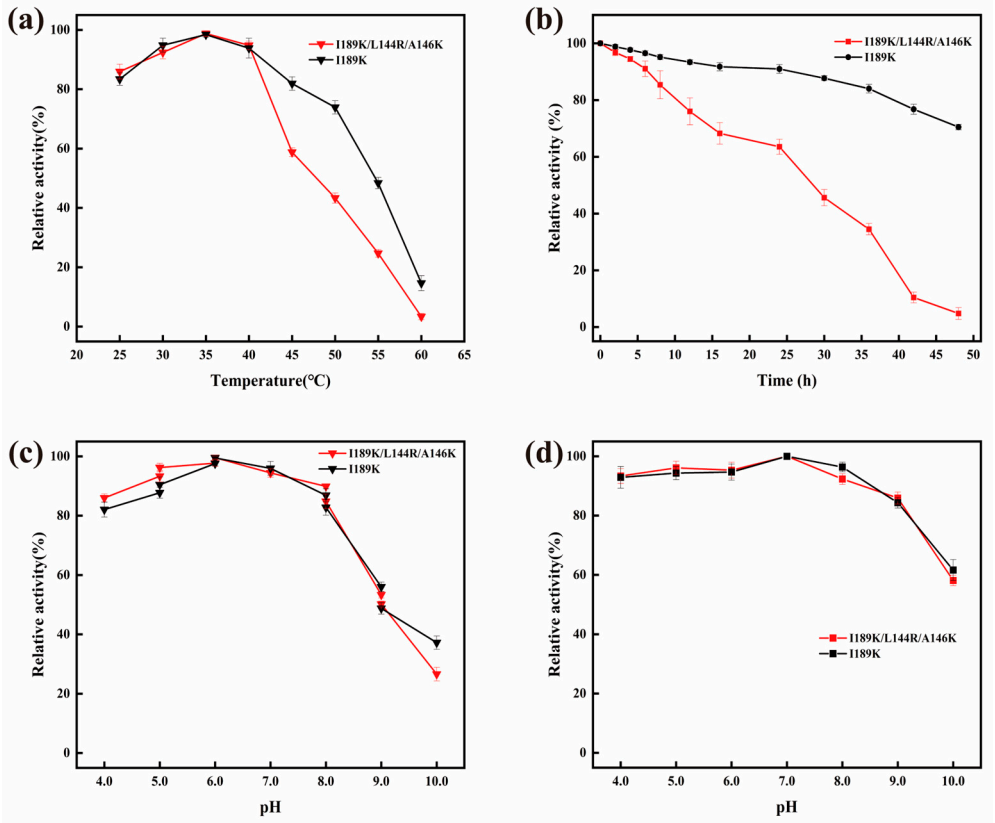


Figure 4. Effects of temperature and pH on the activity and stability of the I189K/L144R/A146K mutant in comparison with I189K: (**a**) optimal temperature for mutants; (**b**) thermal stability at 35 °C over 48 h; (**c**) optimal pH for the mutant; (**d**) pH stability after 24 h incubation.

Analysis of Figure 4c reveals that the mutant I189K/L144R/A146K achieved maximal catalytic activity at pH 6.0, maintaining high activity within the pH range of 5.0 to 6.0, thereby forming a stable activity plateau. Its optimal pH fully coincides with that of the parent enzyme I189K pH (6.0), reflecting its strong catalytic performance under acidic conditions. Thus, the mutant I189K/L144R/A146K inherits and enhances the superior pH characteristics of I189K in determining the enzyme activity–pH curve. Notably, regarding pH stability (Figure 4d), the mutant I189K/L144R/A146K retained more than 80% of its initial activity after incubation across the broad pH range of 5.0 to 9.0. Its stability within the target acidic range (pH 5.0–6.0) was particularly outstanding, remaining consistent with the stability trend of the parent enzyme I189K and significantly outperforming the wild-type enzyme. It should be noted, however, that the reduced long-term thermal stability of the triple mutant does not practically limit its performance under the short reaction times (2.6–20 h) used in our kinetic resolution experiments, as the residual activity remains sufficient to achieve the observed conversions.

In summary, the mutant I189K/L144R/A146K largely preserves the optimal catalytic conditions of the parent enzyme I189K (35 °C, pH 6.0). Its primary advancement lies in further enhancing catalytic efficiency (k_{cat}/K_m) to 273.73 through combinatorial mutation—approximately 4.5-fold that of I189K. Although this improvement is partially accompanied by reduced thermal stability, its operational stability at the mild optimal temperature of 35 °C remains sufficient for conventional industrial batch processes, while

maintaining excellent stability within the critical acidic pH range. Overall, this mutant retains the advantageous framework of I189K in core enzymatic properties while synergistically amplifying catalytic efficiency, thereby offering a superior catalyst candidate for the highly efficient biocatalytic synthesis of moxifloxacin intermediates.

2.5. Enzymatic Catalysis of the Hydrolysis of cis-(±)-1

To evaluate the performance of the resulting mutant in practical applications, this study compared the catalytic efficiency of the enzyme I189K with the mutant I189K/L144R/A146K at different substrate concentrations. The results clearly demonstrate that the mutant I189K/L144R/A146K exhibits superior catalytic performance under all tested conditions compared to the enzyme I189K (Figure S5).

At a substrate concentration of 1 M (Figure 5a), the I189K/L144R/A146K mutant showed an exceptional reaction rate, achieving 50% conversion in approximately 2.6 h—significantly reducing the reaction time compared to the enzyme I189K. This experimental observation aligns perfectly with kinetic parameters: the catalytic efficiency (k_{cat}/K_m) of the I189K/L144R/A146K mutant reached 273.73 min^{-1}·mM^{-1}, which is approximately 4.5-fold that of the enzyme I189K (61.40 min^{-1}·mM^{-1}). The efficiency gain primarily stems from a substantial increase in the k_{cat} value (from 1722.35 min^{-1} to 11,617.28 min^{-1}), indicating marked enhancement in the intrinsic catalytic capacity of each enzyme molecule. Although the K_m value increased, reflecting a moderate decrease in the enzyme's apparent affinity, the dramatic rise in k_{cat} fully compensated for this effect, driving the overall optimization of catalytic efficiency.

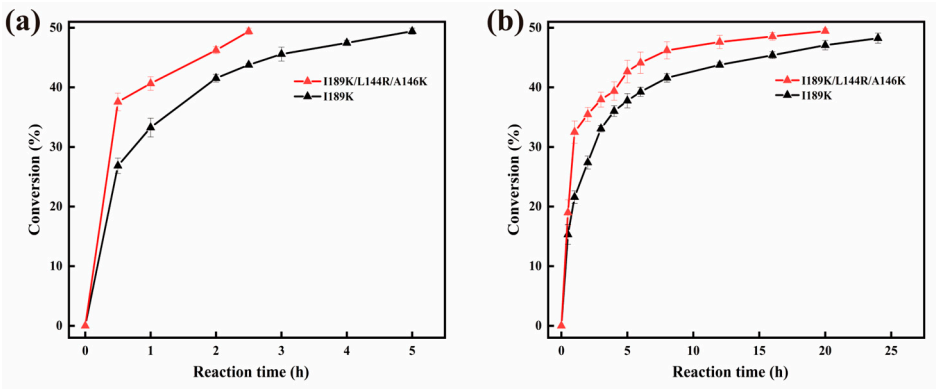


Figure 5. Comparison of enzymatic hydrolysis conversion rates of the I189K/L144R/A146K mutant at different substrate concentrations: (**a**) conversion rate curve at 1 M substrate concentration; (**b**) conversion rate curve at 2 M substrate concentration.

Even at the higher substrate concentration of 2 M (Figure 5b), the mutant I189K/L144R/A146K reached 50% conversion in approximately 20 h, faster than the enzyme I189K—further confirming its catalytic advantage under varying reaction loads. Although reaction rates slowed at high concentrations—potentially due to an "activity–stability tradeoff" and potential substrate inhibition—this did not alter the fundamental conclusion that the I189K/L144R/A146K mutant outperformed the initial mutant across all tested conditions. It is worth noting that under the high substrate concentrations used here (1–2 M), the modest increase in K_m (from 28.05 to 42.44 mM) does not practically limit the reaction rate, as the enzyme is working under substrate-saturating conditions.

For quantitative context, our triple mutant I189K/L144R/A146K exhibits a k_{cat}/K_m of 273.73 min^{-1}·mM^{-1}, which is 4.5-fold higher than that of the parent I189K (61.40 min^{-1}·mM^{-1}). Compared to wild-type CALB, which required 140 h to resolve 0.3 M substrate, our mutant achieves 50% conversion of 1 M substrate in only 2.6 h. Relative to the previously reported I189K

(286-fold improvement over wild-type) [13], our triple mutant, with an additional 4.5-fold higher k_{cat}/K_m over I189K, represents an estimated overall enhancement of approximately 1287-fold in catalytic efficiency compared to the wild-type enzyme.

In summary, the synergistic enhancement of the I189K background through L144R and A146K mutations enabled the constructed I189K/L144R/A146K mutant to achieve a stepwise leap in catalytic efficiency. Its highly efficient and rapid conversion capability at concentrations approaching industrial relevance (1 M) provides strong support for its application as a high-performance biocatalyst in the green synthesis of moxifloxacin intermediates.

2.6. Structural Characterization and Mechanism Elucidation of CALB Mutants Based on Molecular Dynamics Simulations

We constructed a three-dimensional structural model based on the final mutant I189K/L144R/A146K and performed a 100 ns molecular dynamics simulation. The RMSD value of this system stabilized after approximately 40 ns, so we calculated the RMSF of the protein backbone atoms based on the final 30 ns trajectory (Figure S6). By comparing its RMSF with that of the I189K mutant, we observed a significant increase in conformational flexibility within the 143–146 region. This trend is consistent with the previously mentioned findings between the wild-type CALB and the I189K enzyme.

This study identified a CALB forward mutant with significantly enhanced catalytic activity while maintaining enantiomeric selectivity comparable to the enzyme I189K. Through computational simulations, we conducted an in-depth analysis of the complex structures formed between the mutant enzymes and their substrates. Figure 6a,b illustrate the binding conformations of the substrate within the active pockets of the enzyme I189K and the I189K/L144R/A146K mutant. Specifically, the L144R mutation replaces the original hydrophobic side chain with a positively charged polar arginine, while the A146K mutation introduces a longer, similarly positively charged lysine side chain that extends outward from the pocket. The substrate-binding pocket volume was calculated to be 582 $Å^3$ in I189K and 594 $Å^3$ in the I189K/L144R/A146K mutant (Figure 6c,d). Given the inherent uncertainty of volume calculations, this modest increase (~2%) should be interpreted with caution. Thus, this marginal change does not serve as a mechanistic explanation for the enhanced catalytic activity. The experimental kinetic data show that the primary effect of the mutations is on k_{cat}, while K_m values remained within the same order of magnitude. The slightly higher K_m of the triple mutant suggests a modest decrease in apparent affinity, likely due to altered electrostatic interactions from the introduced charged residues. However, this is fully compensated by the dramatic increase in k_{cat}, resulting in a 4.5-fold improvement in catalytic efficiency (k_{cat}/K_m).

Additionally, amino acid residues 144 and 146 are immediately adjacent to the substrate. The combined effect of 144R and 146K brings the substrate closer to the catalytic triad and causes D187 to swing toward H224. In the I189K/L144R/A146K mutant variant, the distance between the oxygen atom of S105 and the hydrogen atom of H224 shortens from 3.5 Å in the enzyme I189K to 2.5 Å. The low-barrier hydrogen bond formed between S105 and H224 facilitates nucleophilic attack, and this substitution alters the ligand binding conformation (Figure S7). The distance r(O-C) between catalytic serine S105 and the acyl carbon atom of the substrate, as well as the distance r(N-O) between the nitrogen atom of active site histidine H224 and the oxygen atom of the alcohol group in the substrate, also undergo significant changes (Figure 6e,f). For the I189K/L144R/A146K mutant, these distances are 2.4 Å and 3.5 Å, respectively, compared to 3.2 Å and 3.8 Å in the enzyme I189K. The shorter nucleophilic attack distances in the I189K/L144R/A146K mutant indicate that the mutant substrate complex represents a more favorable close-attack conformation than the enzyme I189K complex. Similarly, in Shen et al.'s study [13], the I189K mutation also shortened the r(O-C) and r(N-O) distances (from 3.0 Å and 3.3 Å in the wild-type to 2.4 Å

and 3.0 Å, respectively), thereby forming a more favorable attack conformation. This further explains the observed enhancement in catalytic activity.

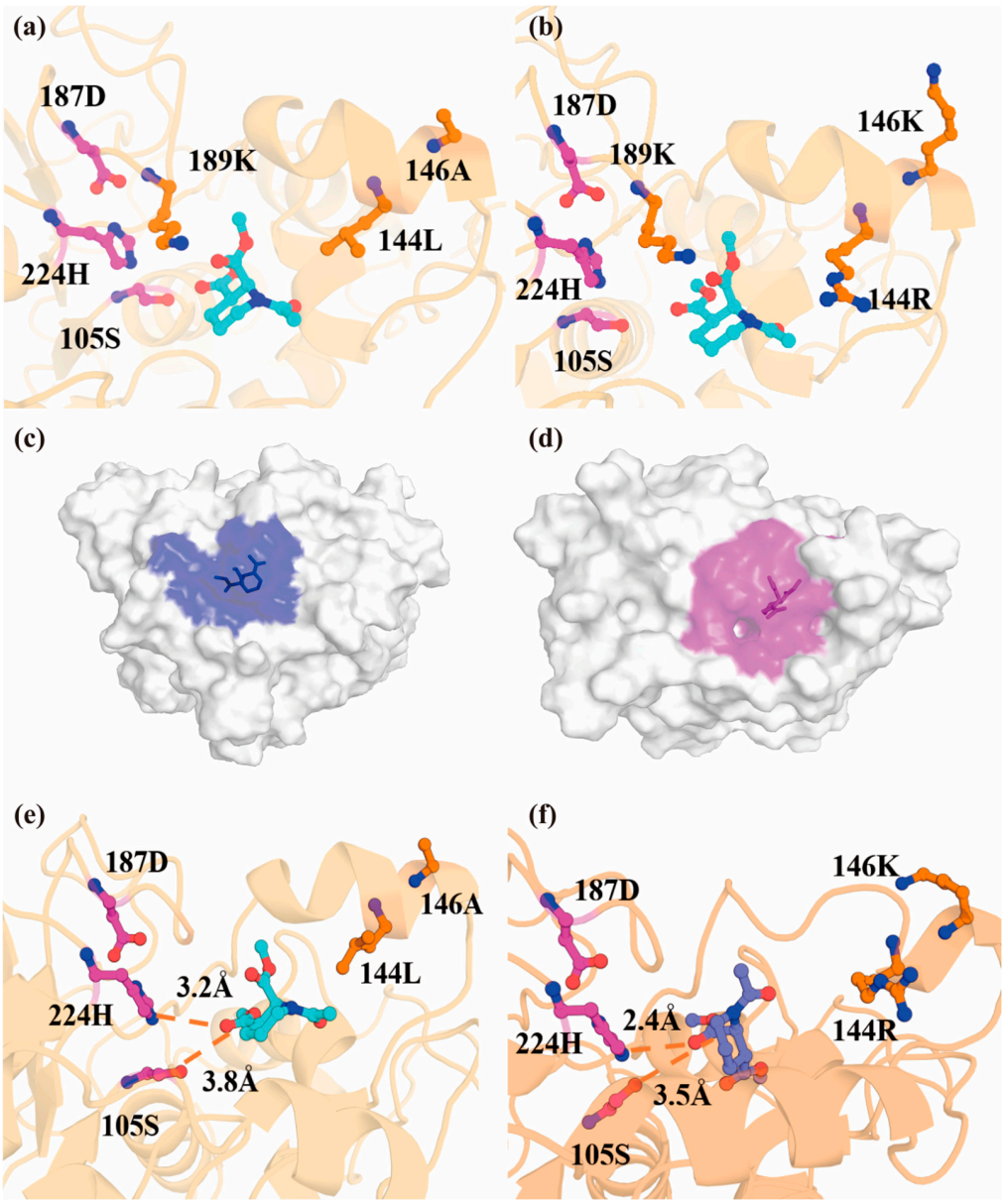


Figure 6. Structural characterization and catalytic mechanism of CAL-B mutants: (**a**) Structural view of the enzyme I189K active pocket. (**b**) Structural view of the mutant I189K/L144R/A146K active pocket, showing the introduced R144 and K146 residues. (**c**) Volumetric representation of the substrate-binding pocket in enzyme I189K; (**d**) the mutant I189K/L144R/A146K showing pocket enlargement upon mutation; (**e**) key catalytic distances in the enzyme I189K and (**f**) the mutant I189K/L144R/A146K complexes: the nucleophilic attack distance between the serine S105 oxygen and the substrate acyl carbon (r(O-C)), and the distance between the histidine H224 nitrogen and the substrate alcohol oxygen (r(N-O)).

Although many previous studies indicated that CALB possesses only a short lip region, Luan and Zhou [19] proposed based on long-term molecular dynamics simulations that a salt bridge can form between D145 on Loop 6 and R309 on the β8 fold in CALB. Simultaneously, hydrophobic interactions among L144, L147, and W155 collectively maintain the open conformation of the lid structure. Furthermore, the hydrophobic residues P143, L144, L147, and V149 on Loop 6 promote the transition of the lid structure toward a closed

state through hydrophobic interactions with V286 and K290 on the α10 helix. Conversely, hydrophobic interactions between A282 and L278 on the α12 helix and Loop-domain residue I189 further strengthen the hydrophobic linkage between Loop 6 and the α10 helix, collectively regulating CALB's structural dynamics and function. The I189K/L144R/A146K mutant constructed in this study may disrupt the local hydrophobic network formed by residues L144, L147, and W155 due to the introduction of positively charged arginine (R144) at position 144, potentially forming new electrostatic interactions with surrounding residues. Simultaneously, the lysine (K146) introduced at position 146 may participate in charge balancing near the active site or form new hydrogen bonds. These combined changes affect the structural dynamics and conformational stability of Loop 6, leading to significant conformational rearrangement in this mutant. The resulting twisted-like state causes lip to adopt a relatively open conformation (Figure S8). This structural alteration facilitates substrate entry and product release, consistent with the experimentally observed increase in k_{cat} for the mutant.

3. Materials and Methods

3.1. Plasmids, Strains, and Chemical Reagents

The substrate *cis*-(±)-1 and the reference samples of the hydrolysis products (2*R*,3*S*)-2 (containing (2*R*,3*S*)-2a and (2*R*,3*S*)-2b) were provided by Taian Havay Chemicals Co., Ltd. (Taian, China). Ampicillin (Amp) and isopropyl-β-D-1-thiogalactopyranoside (IPTG) were purchased from Aladdin (Shanghai, China). All other reagents were commercially available and used directly without further processing. Mutation primers and DNA sequencing were supplied by General Biosystems (Anhui) Corp. Ltd. (Chuzhou, China). Phanta Max Master MIX DNA polymerase, restriction endonuclease *Dpn* I, and the BCA Protein Assay Kit were purchased from Vazyme Biotech Co., Ltd. (Nanjing, China). The pET-25b (+) vector was used for cloning the target gene with *E. coli* DH5α competent cells for plasmid cloning and *E. coli* BL21(DE3) competent cells for protein expression.

3.2. Construction of Mutant Libraries

Site-directed saturation and combinatorial mutagenesis of CALB-I189K were performed using whole-plasmid PCR. The oligonucleotides 1–90 were designed for mutagenesis (Table S1). The CALB-I189K gene was cloned into the pET-25b (+) plasmid, which served as the template for mutant plasmid construction. Whole-plasmid PCR amplification was performed using Phanta Max Master MIX DNA Polymerase (Vazyme, Nanjin, China) under the following conditions: initial denaturation at 95 °C for 3 min; 32 cycles of 95 °C for 15 s, 60 °C for 15 s, 72 °C for 1 min; followed by a final extension at 72 °C for 10 min. The PCR products were digested with *Dpn* I at 37 °C for 30 min and subsequently transformed into *E. coli* BL21 (DE3) competent cells for expression.

3.3. Protein Expression and Purification

Inoculate the recombinant CALB-I189K and its mutants into 30 mL Luria–Bertani (LB) broth with 100 μg/mL ampicillin, and incubate for an overnight period at 37 °C with 180 rpm/min shaking. Further transfer the culture to 150 mL of fresh Terrific Broth (TB) medium with 100 μg/mL ampicillin (2%, *v*/*v*). Upon achieving an optical density (OD_{600}) value within the range of 0.6–0.8, add isopropyl-β-D-1-thiogalactopyranoside (IPTG) to a final concentration of 0.2 mM in the medium. Recombinase expression was induced at 18 °C for 26 h, after which the recombinant cells were collected by centrifugation (8000 rpm, 10 min). The cells pellets were resuspended in 50 mM Na_2HPO_4-NaH_2PO_4 buffer (pH 7.5). Following sonication, the lysates were centrifuged at 12,000 rpm for 10 min to remove cell debris.

The supernatants were purified using an ÄKTAgo system (Cytiva, Marlborough, MA, USA) equipped with the Ni-NTA resin affinity column (GE Healthcare, Chicago, IL, USA), as described previously. Protein purity was evaluated by SDS-PAGE, and protein concentration was determined using a BCA Protein Assay Kit (Vazyme, Nanjin, China) according to the manufacturer's instructions.

3.4. High-Throughput Screening of Positive Mutants

Individual colonies were manually picked and inoculated into 1 mL of LB medium containing 100 μg/mL ampicillin in each well (2 mL capacity) of a 96-well deep-well plate. The cultures were incubated at 37 °C for 8 h, after which the temperature was reduced to 18 °C and 2 μL of IPTG was added to each well to a final concentration of 0.2 mM. Following incubation at 18 °C for 12 h, 200 μL of each culture was mixed with 200 μL of 30% glycerol in a new 96-well plate and stored at −80 °C. The original plate was centrifuged at 3000× *g* for 30 min, and the supernatant was discarded. The cell pellets in each well were resuspended in 400 μL of 5 mM Tris-HCl buffer (pH 8.5). Hydrolysis reactions were performed in a 96-well microplate containing 100 μL of the cell suspension, 20 μL of indicator solution (0.5 mg/mL bromothymol blue dissolved in 5 mM Tris-HCl buffer, pH 8.5), and 100 μL of substrate solution (100 mM calcium chloride and 20 g/L (2*R*,3*S*)-1 mixed with (2*S*,3*R*)-1 dissolved in 5 mM Tris-HCl buffer, pH 8.5). The substrate and indicator solutions were first added to each well of a 96-well microplate; the liquids in each well were then mixed, followed by the addition of the cell suspension to initiate the reaction. The reactions were incubated at 37 °C. The entire primary screening procedure (colony picking, culture, induction, and colorimetric assay) was independently performed three times, and only clones showing faster color change than the I189K control in at least two of the three runs were selected as primary hits for further HPLC validation. Mutants exhibiting enhanced activity and high enantiomeric selectivity were identified by color change [24] and further confirmed by HPLC analysis.

3.5. Standard Enzyme Activity Assay and Kinetic Characterization

Enzyme activity was measured by determining the conversion rate of 50 mmol·L^{-1} *cis*-(±)-1 to (2*R*,3*S*)-1. The reaction system (1 mL) comprised 100 mmol·L^{-1} sodium phosphate buffer (pH 7.0), 50 mmol·L^{-1} *cis*-(±)-1, and 10 μg of pure enzyme. The reaction mixture was incubated at 35 °C for 30 min and then terminated by the addition of 30 μL of 4 mol·L^{-1} HCl. The products were extracted with 1 mL tert-butyl methyl ether (TBME). A 500 μL aliquot was dried to dryness with anhydrous sodium sulfate. The samples were analyzed by HPLC to evaluate conversion and stereoselectivity. One unit (U) of enzyme was defined as the amount of enzyme required to hydrolyze 1 μmol (2*R*,3*S*)-1 per minute at pH 7.0 and 35 °C.

The kinetic parameters of the purified enzyme towards *cis*-(±)-1 were determined by measuring the initial reaction rates at substrate concentrations ranging from 2 to 200 mM. The values of V_{max} and K_m were calculated by nonlinear regression analysis based on the Michaelis–Menten equation, along with their corresponding error margins.

3.6. Effects of Temperature and pH on Mutant Activity and Stability

The effects of temperature and pH on enzyme activity were evaluated by measuring the initial hydrolysis rate of *cis*-(±)-1 under different reaction conditions. The optimal temperature for the mutants was determined under standard assay conditions at various temperatures (25–60 °C). For thermostability analysis, purified enzyme was incubated at the optimal temperature for 48 h, and the residual activity measured at various time intervals. The optimal pH for the mutants was determined at 35 °C in the following buffers (final concentration 100 mM): sodium acetate (pH 4.0–5.0), sodium citrate (pH

5.0–6.0), sodium phosphate (pH 6.0–8.0), Tris-HCl (pH 8.0–9.0), and sodium bicarbonate (pH 9.0–10.0). To assess pH stability, purified enzyme was incubated at 4 °C for 24 h in various buffers (100 mM, pH 4.0–10.0), followed by measurement of residual activity.

3.7. HPLC Detection

HPLC analysis was performed using a Waters Alliance®2695 system (Waters Technologies (Shanghai) Ltd., Shanghai, China) with a Waters 2487 UV detector [25,26]. Separation was achieved on a Chiralpak®IG column (φ4.6 mm × 250 mm, 5 μm; Daicel, Tokyo, Japan). The mobile phase consisted of 60% *n*-hexane and 40% ethanol, delivered at a flow rate of 1.0 mL·min^{-1}. Detection was carried out at a wavelength of 220 nm, and the column temperature was maintained at 30 °C. Each sample (10 μL) was injected, with retention times of 10.5 min for (2*R*,3*S*)-1 and 13.6 min for (2*S*,3*R*)-1. All samples were analyzed in duplicate.

3.8. Determination of Enantioselectivity (E Value)

The *E* value was calculated using the following equation [27]:

$$E = \frac{\ln\left[1-c\left(1+ee_p\right)\right]}{\ln\left[1-c\left(1-ee_p\right)\right]}$$

where *c* is the conversion and ee_p is the enantiomeric excess of the product. Both conversion and product ee were determined by chiral HPLC as described above.

3.9. Enzymatic Hydrolysis of cis-(±)-1 by Mutants

To further explore its industrial potential, the enzymatic conversion efficiency of *cis*-(±)-1 was evaluated at concentrations of 1.0 and 2.0 mol·L^{-1}. The reaction was carried out using 0.1 g·L^{-1} of purified CALB-I189K mutant enzyme in 30 mL of phosphate buffer (pH 6.0) with magnetic stirring at 35 °C. During the reaction, 3 mol·L^{-1} NaOH was added to automatically maintain the reaction pH at 6.0, and samples were taken periodically to determine the conversion rate.

3.10. Molecular Docking and Molecular Dynamics Simulation

In this study, the wild-type CALB structure was obtained from the Protein Data Bank (PDB code: 1TCA), and the three-dimensional structures of the target proteins were predicted using the AlphaFold2 artificial intelligence model [28]. Based on these predicted structures, molecular docking calculations were performed with the AutoDock Vina 1.2.0 program to identify energetically optimal binding conformation of candidate molecules [29]. To further assess the stability of these complexes under near-physiological conditions and to investigate the details of their dynamic interactions, molecular dynamics simulations were conducted on the optimal conformation system obtained from docking. Molecular dynamics simulations were performed using GROMACS 2025.2 software [30] with the AMBER14 [31,32] force field. Atomic charges were calculated using the RESP method in Gaussian, while the ACPYPE program generated force field parameters for the simulation system. Hydrogen atoms were added to the enzyme structure using the pdb2gmx module in GROMACS. Water molecules were represented by the TIP3P model, and the docked protein–ligand complex was confined within a 10 × 10 × 10 nm^3 cubic box with periodic XYZ boundary conditions. Prior to initiating MD simulations, energy minimization was performed using the conjugate gradient method. The step size was set to 0.001 nm, with a cycle limit of 50,000 steps. Minimization was considered converged when the minimum force fell below 500 kJ·mol^{-1}·nm^{-1}. Van der Waals interactions are calculated using the cutoff method, while atomic electrostatic interactions were computed via the Particle Mesh Ewald (PME) method, with both the cutoff and PME distances set to 1.2 nm [33]. The system

was then equilibrated at 1.0 bar pressure to achieve the desired density. Temperature and pressure were maintained using the V-rescale and Parrinello–Rahman methods, respectively, with a time constant of 1.0 ps and a compressibility of 4.5×10^{-5} bar^{-1}. All systems were equilibrated for 100 ps with a time step of 0.002 ps, and the final production simulation was run for 100 ns. Hydrogen bonds were constrained using the LINCS (Linear Constraint Solver) algorithm [34]. Final configurations were exported from GROMACS and visualized using VMD 1.9.3 software [35].

4. Conclusions

This study successfully constructed and systematically characterized the CALB mutant I189K/L144R/A146K, achieving significant progress in catalyzing the synthesis of the key chiral intermediate for moxifloxacin. Experimental results indicate that this mutant retains the excellent catalytic properties of the I189K (under optimal conditions: 35 °C, pH 6.0). Through the synergistic effects of L144R and A146K, the catalytic efficiency (k_{cat}/K_m) is further enhanced to 273.73, representing approximately 4.5-fold that of the I189K. At an enzyme loading of 0.1 g/L and a substrate concentration of 1 M, it achieves 50% conversion within 2.6 h, demonstrating highly efficient kinetic resolution capability. Although long-term reaction rates are limited at high substrate concentrations (2 M) due to an activity–stability trade-off, its high activity under target acidic conditions and excellent pH stability provide a robust candidate catalyst for developing efficient, green industrial biosynthetic processes for moxifloxacin intermediates, offering significant application prospects. Nevertheless, we acknowledge that additional studies on operational stability (e.g., enzyme recycling, long-term continuous operation, and scale-up) are required to fully establish industrial feasibility.

Supplementary Materials: The following supporting information can be downloaded at: https://www.mdpi.com/article/10.3390/catal16050377/s1, Table S1: Primer sequences for constructing mutants based on the CAL-B-I189K template; Figure S1: RMSD of CAL-B-I189K during molecular dynamics simulation; Figure S2: Comparison of RMSD and RMSF between Wild-Type CAL-B and CAL-B-I189K; Figure S3: High-throughput colorimetric screening of the mutant library; Figure S4: SDS-PAGE analysis of purified CALB variants. Lane M: protein marker; Lane 1: purified I189K/L144R/A146K; Lane 2: purified I189K; Figure S5: High-performance liquid chromatography monitoring of the hydrolysis reaction catalyzed by the CAL-B variant; Figure S6: Comparison of RMSD and RMSF between I189K and I189K/L144R/A146K; Figure S7: Distance changes at the catalytic site S105-H224 in CAL-B mutants; Figure S8: I189K/L144R/A146K mutations disrupt the hydrophobic network and induce conformational opening of Loop 6.

Author Contributions: Conceptualization and writing—original draft, S.W. and B.W.; investigation and writing—original draft, M.A.; data curation, Y.Z.; visualization, S.W.; writing—review and editing and supervision, J.X. and C.C. All authors have read and agreed to the published version of the manuscript.

Funding: This work was supported by National Key Research and Development Program of China (2025YFE0215600) and the National Natural Science Foundation Youth Fund (22308159).

Data Availability Statement: All data were included in the main text and Supplementary File. Raw data can be sent upon request from the corresponding authors.

Conflicts of Interest: Author Yilin Zhang was employed by the company Taian Havay Chemicals Co., Ltd. The remaining authors declare that the research was conducted in the absence of any commercial or financial relationships that could be construed as a potential conflict of interest.

References

1. Gillespie, S.H.; Crook, A.M.; McHugh, T.D.; Mendel, C.M.; Meredith, S.K.; Murray, S.R.; Pappas, F.; Phillips, P.P.; Nunn, A.J. Four-month moxifloxacin-based regimens for drug-sensitive tuberculosis. *N. Engl. J. Med.* **2014**, *371*, 1577–1587. [CrossRef]
2. Xu, Y.H.; Li, D.; Liu, X.Y.; Li, Y.Z.; Lu, J. High performance liquid chromatography assay with ultraviolet detection for moxifloxacin: Validation and application to a pharmacokinetic study in Chinese volunteers. *J. Chromatogr. B* **2010**, *878*, 3437–3441. [CrossRef]
3. Pallavicini, M.; Bolchi, C.; Fumagalli, L.; Piccolo, O.; Valoti, E. Highly efficient racemisation of a key intermediate of the antibiotic moxifloxacin. *Tetrahedron Asymmetry* **2011**, *22*, 379–380. [CrossRef]
4. Li, G.; Wu, L.; Fu, Q.; Tang, Z.; Zhang, X. First way of enantioselective synthesis of moxifloxacin intermediate. *Sci. China Chem.* **2013**, *56*, 307–311. [CrossRef]
5. Lorenz, H.; Seidel-Morgenstern, A. Processes to Separate Enantiomers. *Angew. Chem. Int. Ed.* **2014**, *53*, 1218–1250. [CrossRef]
6. Fogal, S.; Motterle, R.; Arvotti, G.; Galvagni, M.; Castellin, A.; Bergantino, E. Enzymatic resolution of cis-dimethyl 1-acetylpiperidine-2,3-dicarboxylate for fine chemicals preparation. *J. Biotechnol.* **2010**, *150*, S382. [CrossRef]
7. Tao, J.; Liang, X.; Jiang, X.; Le, Y. Preparation of Moxifloxacin Side Chain by Biological Method. CN 106399418 A, 25 September 2020.
8. Ramesh, P.; Harini, T.; Fadnavis, N.W. Efficient Resolution of *cis*-(±)-Dimethyl 1-Acetylpiperidine-2,3-dicarboxylate with Soluble *Candida antarctica* Lipase B (CAL B). *Org. Process Res. Dev.* **2014**, *19*, 296–301. [CrossRef]
9. Cai, X.; Shen, J.-W.; Qiang, Y.; Hua, J.; Ma, Z.-Q.; Liu, Z.-Q.; Zheng, Y.-G. Efficient Activity Enhancement of a Lipase from *Sporisorium reilianum* for the Synthesis of a Moxifloxacin Chiral Intermediate via Rational Design. *Engineering* **2022**, *19*, 207–216. [CrossRef]
10. Reetz, M.T. Directed Evolution of Enantioselective Enzymes as Catalysts for Organic Synthesis. In *Advances in Catalysis*; Gates, B.C., Knözinger, H., Eds.; Academic Press: Cambridge, MA, USA, 2006; pp. 1–69.
11. Böttcher, D.; Bornscheuer, U.T. Protein engineering of microbial enzymes. *Curr. Opin. Microbiol.* **2010**, *13*, 274–282. [CrossRef] [PubMed]
12. Chen, Z.; Zeng, A.P. Protein engineering approaches to chemical biotechnology. *Curr. Opin. Biotechnol.* **2016**, *42*, 198–205. [CrossRef]
13. Shen, J.-W.; Qi, J.-M.; Zhang, X.-J.; Liu, Z.-Q.; Zheng, Y.-G. Significantly increased catalytic activity of *Candida antarctica* lipase B for the resolution of *cis*-(±)-dimethyl 1-acetylpiperidine-2,3-dicarboxylate. *Catal. Sci. Technol.* **2018**, *8*, 4718–4725. [CrossRef]
14. Lu, Y.; Meng, S.; Guan, X.; He, P.; Zhao, D. A Rapid, High-Throughput Method for the Construction of Mutagenesis Libraries. *Biomolecules* **2025**, *15*, 1511. [CrossRef]
15. Gagné, D.; Charest, L.-A.; Morin, S.; Kovrigin, E.L.; Doucet, N. Conservation of Flexible Residue Clusters among Structural and Functional Enzyme Homologues. *J. Biol. Chem.* **2012**, *287*, 44289–44300. [CrossRef] [PubMed]
16. Hegazy, R.; Richard, J.P. The Role of Protein Side Chains in Enzyme-Activating Conformational Changes: Lessons from Studies on Variant Enzymes. *Chem. Rev.* **2025**, *125*, 11524–11566. [CrossRef] [PubMed]
17. Rivoire, O. A role for conformational changes in enzyme catalysis. *Biophys. J.* **2024**, *123*, 1563–1578. [CrossRef]
18. Stauch, B.; Fisher, S.J.; Cianci, M. Open and closed states of *Candida antarctica* lipase B: Protonation and the mechanism of interfacial activation. *J. Lipid Res.* **2015**, *56*, 2348–2358. [CrossRef] [PubMed]
19. Luan, B.; Zhou, R. A novel self-activation mechanism of *Candida antarctica* lipase B. *Phys. Chem. Chem. Phys.* **2017**, *19*, 15709–15714. [CrossRef]
20. Suplatov, D.A.; Besenmatter, W.; Švedas, V.K.; Svendsen, A. Bioinformatic analysis of alpha/beta-hydrolase fold enzymes reveals subfamily-specific positions responsible for discrimination of amidase and lipase activities. *Protein Eng. Des. Sel.* **2012**, *25*, 689–697. [CrossRef]
21. Lu, X.; Liu, S.; Feng, Y.; Rao, S.; Zhou, X.; Wang, M.; Du, G.; Chen, J. Enhanced thermal stability of *Pseudomonas aeruginosa* lipoxygenase through modification of two highly flexible regions. *Appl. Microbiol. Biotechnol.* **2014**, *98*, 1663–1669. [CrossRef]
22. Radojković, M.; Koene, S.F.; Chikunova, A.; Florea, B.I.; Natarajan, S.V.; Boyle, A.L.; Ubbink, M. Phosphate ions modulate enzyme activity and epistatic effects in two clavulanic acid-resistant β-lactamase mutants. *Protein Sci.* **2025**, *34*, e70325. [CrossRef]
23. Dong, F.; Zhang, M.; Ma, R.; Lu, C.; Xu, F. Insights of conformational dynamics on catalytic activity in the computational stability design of *Bacillus subtilis* LipA. *Arch. Biochem. Biophys.* **2022**, *722*, 109196. [CrossRef]
24. Jiang, H.; Xia, X.X.; Feng, Y.; Zhong, J.J.; Qian, Z.G. Development of a robust system for high-throughput colorimetric assay of diverse amino acid decarboxylases. *Process Biochem.* **2017**, *60*, 27–34. [CrossRef]
25. Shen, J.W.; Cai, X.; Dou, B.J.; Qi, F.Y.; Zhang, X.J.; Liu, Z.Q.; Zheng, Y.G. Expression and characterization of a CALB-type lipase from *Sporisorium reilianum* SRZ2 and its potential in short-chain flavor ester synthesis. *Front. Chem. Sci. Eng.* **2020**, *14*, 868–879. [CrossRef]
26. Shen, J.W.; Qi, J.M.; Zhang, X.J.; Liu, Z.Q.; Zheng, Y.G. Efficient Resolution of *cis*-(±)-Dimethyl 1-Acetylpiperidine-2,3-dicarboxylate by Covalently Immobilized Mutant *Candida antarctica* Lipase B in Batch and Semicontinuous Modes. *Org. Process Res. Dev.* **2019**, *23*, 1017–1025. [CrossRef]

27. Rakels, J.L.L.; Straathof, A.J.J.; Heijnen, J.J. A simple method to determine the enantiomeric ratio in enantioselective biocatalysis. *Enzyme Microb. Technol.* **1993**, *15*, 1051–1056. [CrossRef]
28. Abramson, J.; Adler, J.; Dunger, J.; Evans, R.; Green, T.; Pritzel, A.; Ronneberger, O.; Willmore, L.; Ballard, A.J.; Bambrick, J.; et al. Accurate structure prediction of biomolecular interactions with AlphaFold 3. *Nature* **2024**, *630*, 493–500. [CrossRef] [PubMed]
29. Rizvi, S.M.; Shakil, S.; Haneef, M. A simple click by click protocol to perform docking: AutoDock 4.2 made easy for non-bioinformaticians. *EXCLI J.* **2013**, *12*, 831–857.
30. Abraham, M.J.; Murtola, T.; Schulz, R.; Páll, S.; Smith, J.C.; Hess, B.; Lindahl, E. GROMACS: High performance molecular simulations through multi-level parallelism from laptops to supercomputers. *SoftwareX* **2015**, *1–2*, 19–25. [CrossRef]
31. Cornell, W.D.; Cieplak, P.; Bayly, C.I.; Gould, I.R.; Merz, K.M.; Ferguson, D.M.; Spellmeyer, D.C.; Fox, T.; Caldwell, J.W.; Kollman, P.A. A Second Generation Force Field for the Simulation of Proteins, Nucleic Acids, and Organic Molecules. *J. Am. Chem. Soc.* **1995**, *117*, 5179–5197. [CrossRef]
32. Case, D.A.; Cheatham, T.E., 3rd; Darden, T.; Gohlke, H.; Luo, R.; Merz, K.M., Jr.; Onufriev, A.; Simmerling, C.; Wang, B.; Woods, R.J. The Amber biomolecular simulation programs. *J. Comput. Chem.* **2005**, *26*, 1668–1688. [CrossRef]
33. Darden, T.A.; York, D.M.; Pedersen, L.G. Particle mesh Ewald: An N·log(N) method for Ewald sums in large systems. *J. Chem. Phys.* **1993**, *98*, 10089–10092. [CrossRef]
34. Hess, B. P-LINCS: A Parallel Linear Constraint Solver for Molecular Simulation. *J. Chem. Theory Comput.* **2008**, *4*, 116–122. [CrossRef] [PubMed]
35. Park, H.J.; Park, K.; Kim, Y.H.; Yoo, Y.J. Computational approach for designing thermostable *Candida antarctica* lipase B by molecular dynamics simulation. *J. Biotechnol.* **2014**, *192*, 66–70. [CrossRef] [PubMed]

Disclaimer/Publisher's Note: The statements, opinions and data contained in all publications are solely those of the individual author(s) and contributor(s) and not of MDPI and/or the editor(s). MDPI and/or the editor(s) disclaim responsibility for any injury to people or property resulting from any ideas, methods, instructions or products referred to in the content.